The Stability of Euclidean Wormholes

James Chryssanthacopoulos[1]

[1]University of Padova, Padova PD, Italy

`jamespeter.chryssanthacopoulos@studenti.unipd.it`

Abstract. *Wormholes are intriguing solutions to general relativity that connect asymptotic regions of spacetime. While many types of wormholes have been studied for decades, Euclidean wormholes have received renewed interest because of their role in showing how information can be recovered from a black hole. Another related issue that wormholes raise is the inability to factorize the gravitational path integral between two geometries if a wormhole connects them. In AdS/CFT, this would imply that the bulk is represented by an ensemble of quantum field theories on the boundary, which defies the traditional understanding of the correspondence. This problem is only relevant if the wormhole is stable, or free of negative modes. This report identifies wormhole solutions in a representative low-energy model inspired by string theory and analyzes its negative modes. Implications for the factorization problem are discussed.*

1. Introduction

In general relativity, the geometry of spacetime is a dynamic field that changes depending on the matter and energy it contains. Classical solutions to general relativity, wormholes are geometries that connect two asymptotic regions of spacetime [1]. Historically, wormhole solutions arose in the context of black holes, connecting two regions of the spacetime, but wormholes can represent more general geometries. Whatever the kind of wormhole, they are generally not humanly traversable unless supported by some exotic matter field. Although they have been studied for decades, wormholes have received renewed interest because of their role in raising and resolving issues in quantum gravity.

One aspect of quantum gravity that wormholes complicate is the AdS/CFT correspondence. A concrete example of the holographic principle, the AdS/CFT correspondence establishes a connection between a gravitational system in asymptotically anti-de Sitter space and a conformal field theory defined on its boundary [2]. Specifically, the correspondence equates the sum of all geometries in the gravitational theory to the partition function of the quantum field theory on the boundary. The sum of all geometries is captured by the path integral over all spacetime configurations. This path integral is usually taken over configurations that have a single compact boundary. The challenge arises when the gravitational theory has multiple boundaries, as in the case of wormholes. In that instance, AdS/CFT equates the gravitational theory with distinct quantum field theories over the different boundaries, but the presence of wormholes implies a correlation between these theories that is not accounted for [3].

A closely related issue that wormholes raise concerns the ability to factor path integrals over geometries with multiple boundaries, depicted in Figure 1. Consider the geometry with a single boundary represented by the first line. Let $\langle Z \rangle$ be the path integral over all configurations terminating in that boundary. If the geometry is duplicated, as

shown on the second line, its path integral should be the product of those of the disconnected geometries, $\langle Z^2 \rangle = \langle Z \rangle^2$. The wormhole connecting the boundaries adds a contribution to the path integral that violates this factorization. In the context of AdS/CFT, this inability to factor the path integral means there are correlations between observables on the two boundaries in the gravitational theory, which implies the presence of correlations between the corresponding quantum field theories.

Figure 1. The path integral over all geometries with two boundaries does not factorize if a wormhole connecting the boundaries is present. This figure is adapted from [4].

While wormholes challenge the traditional understanding of AdS/CFT, it is unclear the extent to which wormhole solutions contribute to the full calculation of the path integral. The path integral over all geometries is given by

$$Z = \int \mathcal{D}g \, e^{iS[g]},$$

where g is the metric tensor and $S[g]$ is the action functional of the theory for a given metric. Since the exponential is an oscillating function, it is common to perform a Wick rotation, introducing the Euclidean time, $t = -i\tau$. The path integral becomes

$$Z = \int \mathcal{D}g \, e^{-S[g]}.$$

Although the integral is performed over all metrics consistent with the boundary conditions, the presence of the minus sign in the exponential means that the integral is dominated by metrics that minimize the action, as shown in Figure 2. Wormholes are given by metrics that are usually found by solving the Einstein equations, but these solutions extremize the action, not necessarily minimize it. If a wormhole solution is a maximum of the action, it may not contribute significantly to the overall path integral. In that case, its role in the problems just described may be limited.

Wormholes that arise from extremizing the action in Euclidean signature are called Euclidean wormholes. Unlike wormholes obtained in Lorentzian signature, they do not necessarily correspond to wormholes that physical exist in the universe, which is described by a Lorentzian metric. Instead, they represent more formal and technical solutions that may dominate the gravitational path integral. One way of determining whether
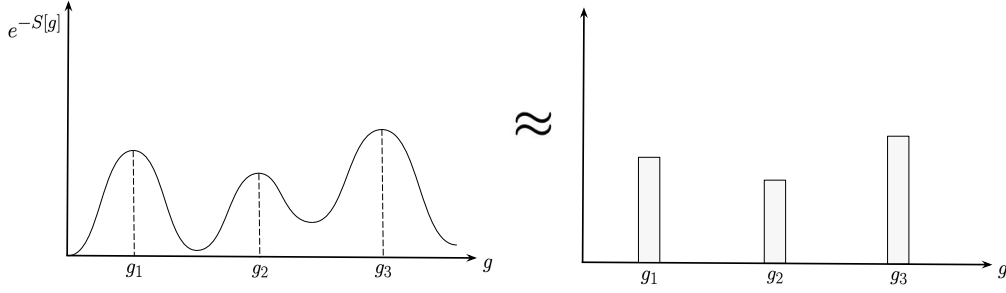
Figure 2. The gravitational path integral is the sum over all geometries, but if the configuration space is dominated by a few points with low action, the path integral can be approximated by the sum only over those metrics.

a wormhole is dominant is by checking if it is unstable when perturbed. This involves expressing the action in terms of fluctuations of the metric around the wormhole solution and checking whether it is has negative eigenvalues. These negative modes are not expected to dominate when integrated over nearby configurations in the path integral. In this way, understanding negative modes is crucial in assessing the importance of wormholes in quantum gravity.

One major reason why wormholes are important in quantum gravity is because they help to explain how information is recovered from a black hole. According to general relativity, anything that falls into a black hole cannot be recovered, but this conflicts with quantum mechanics, which conserves information. Combining general relativity and quantum mechanics semiclassically, it was shown that a black hole emits radiation, as shown in Figure 3. At the event horizon, one particle in a particle-antiparticle pair formed from the vacuum falls into the black hole, while the other is emitted. If the infalling particle is forever trapped inside the black hole, the entropy of the emitted radiation continuously increases. Since the AdS/CFT correspondence regards a black hole as a quantum system, information should be conserved and the entropy should eventually decrease. This evolution of entropy that increases, then decreases, is known as the Page curve, depicted in Figure 4 [5]. To reproduce the Page curve, wormholes are needed to compute the entanglement entropy of the radiation.

The entropy of black hole radiation is calculated using holography. As already mentioned, holography relates a gravitational system to a quantum field theory in one fewer dimension. More concretely, there is a mapping between fields in the bulk, and gauge-invariant operators on the boundary. One example of this mapping is the duality between the bulk metric and the stress tensor on the boundary [1]. Generally, correlation functions of operators on the boundary can be computed from bulk fields. This is especially useful when the boundary theory is strongly coupled, which may correspond to a classical bulk theory with a well-known solution. Another example of the holographic mapping involves quantum information. One measure of quantum information of a boundary region A is the von Neumann entropy

$$S_A = -\text{Tr}(\rho_A \log \rho_A),$$

where ρ_A is the reduced density matrix of the region computed by tracing over the degrees of freedom outside of A, $\rho_A = \text{Tr}_{\bar{A}}(\rho)$. On the gravitational side, the entropy can be
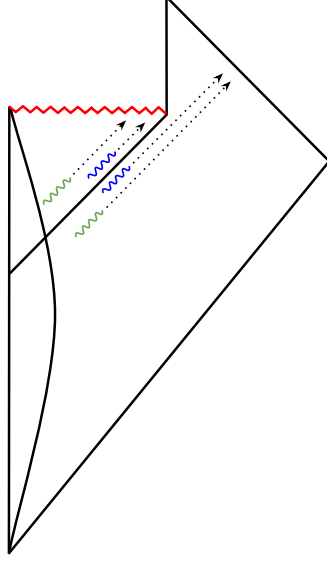
Figure 3. A black hole formed from collapsing matter emits radiation at the event horizon. One particle escapes to asymptotically Minkowski space, while the other falls into the black hole. This figure is adapted from [6].

computed using the Ryu-Takayanagi formula [7]

$$S_A = \frac{\text{Area}(\gamma_A)}{4G_N},$$

where γ_A is the codimension-two hypersurface in the bulk with minimal area that shares the same boundary as A, among other requirements. This geometry is depicted schematically in Figure 5.

When applied to black hole radiation, the Ryu-Takayanagi formula does not provide the entropy of the radiation, but reflects the entropy of the overall gravitational system that contains a black hole. In this way, it is a generalization of the entropy of a black hole in terms of the area of the event horizon [8]. To account for the actual quantum effects of radiation in the bulk, an additional contribution needs to be added

$$S_A = \min\left[\frac{\text{Area}(\gamma_A)}{4G_N} + S_{\text{bulk}}\right],$$

where S_{bulk} is the entanglement of the radiation induced by the presence of the surface γ_A. The minimization is carried out over all possible surfaces satisfying the constraints.

While the quantum-corrected Ryu-Takayanagi incorporates the entropy of matter fields, it is insufficient to model the entropy of radiation during black hole evaporation. That is because as the black hole shrinks, the entropy of the radiation decreases, but S_{bulk} continues to grow. To account for entanglement with radiation in the black hole interior, the entropy is given by

$$S_{\text{rad}} = \min_X\left\{\text{ext}_X\left[\frac{\text{Area}(X)}{4G_N} + S_{\text{sc}}(\Sigma_{\text{rad}} \cup \Sigma_{\text{island}})\right]\right\}, \tag{1}$$
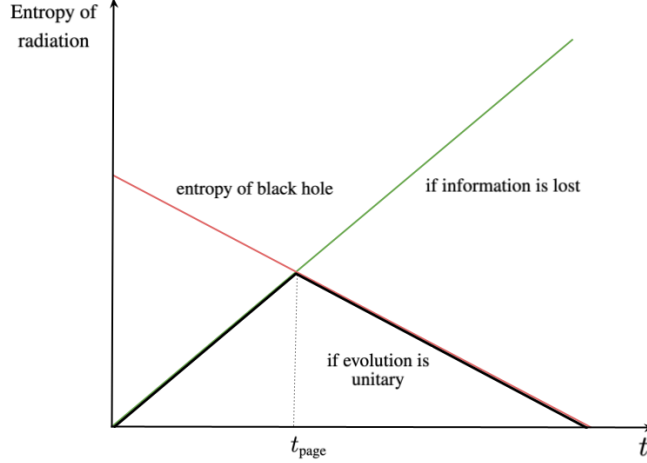
Figure 4. The entropy of black hole radiation initially increases, then starts to decrease when the entropy of the radiation equals that of the black hole. If information is lost inside the black hole, the radiation entropy will continue to increase, but if information is recovered during evaporation, the radiation entropy cannot exceed that of the black hole and starts to decrease.

where the extremization is performed over a general surface X [9]. The semiclassical entropy S_{sc} is computed over the union of two disconnected regions, shown in Figure 6. The region Σ_{rad} encompasses the area from a given cutoff surface to the exterior boundary, while Σ_{island} encompasses the region from the surface X to the interior boundary. As the black hole continues to evaporate, Σ_{island} grows, allowing the entropy to decrease. Intuitively, the center of the black hole becomes identified with the outgoing radiation, although it is separated across the event horizon.

To derive the island formula of Equation 1, wormholes play a crucial role. The semiclassical entropy of the radiation can be computed from its density matrix prepared using the gravitational path integral. Specifically, if the initial state of radiation is given by the wavefunction $|\Psi_i\rangle$, the amplitude of transitioning to the final state $|\Psi_f\rangle$ is given by the path integral

$$\langle \Psi_f | \Psi_i \rangle = \int_{g_i}^{g_f} \mathcal{D}g \, e^{-S[g]},$$

where g_i and g_f are the metrics corresponding to the geometries of the initial and final states, respectively. The elements of the density matrix are then

$$\rho_{ab} = \langle \Psi_a | \Psi_i \rangle \langle \Psi_i | \Psi_b \rangle,$$

which is represented in Figure 7 as two black holes glued together with exterior geometries g_a and g_b. From the density matrix, the entropy can be computed

$$S = (1 - n\partial_n) \log \mathrm{Tr}[\rho^n] \Big|_{n=1}.$$

This calculation can be viewed as replicating the system n times and summing over the different ways of connecting the black hole interior. Consider the case where $n = 2$. There are two main saddles, one where the copies are disconnected and the
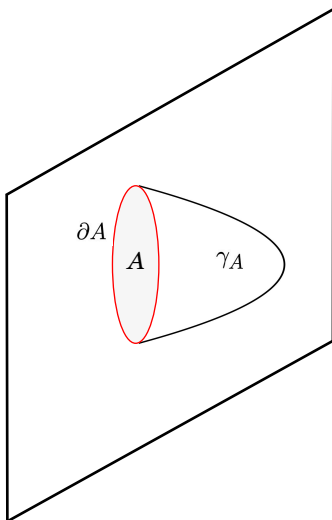
5

Figure 5. The entanglement entropy of quantum fields on A can be computed from the area of the codimension-two hypersurface in the bulk that shares the same boundary.

other when they are connected by a wormhole, depicted in Figure 8. The entropy of the disconnected saddle grows linearly in time. The entropy of the wormhole is initially lower because the path integral incurs an extra factor of e^{-G}, where G is the genus of the wormhole. At later times, the disconnected saddle becomes heavily suppressed by the kinematics, allowing the wormhole saddle to dominate. Because the presence of the wormhole makes the state of the radiation pure, it drives the entropy down to zero. This rising, then falling, behavior of the entropy exactly captures the trend of Equation 1 and is due to the competition between disconnected and wormhole solutions.

The previous discussion highlights the importance of the path integral in calculating the entropy, but wormholes only contribute significantly to the path integral if they are stable, or free of negative modes. Recent work by Marolf and Santos has analyzed the stability of several Euclidean wormhole models in asymptotically anti-de Sitter space [4]. One of the simplest models they analyzed involves three $U(1)$ gauge fields with two spherical boundaries. To apply the AdS/CFT correspondence, the model needs to embed into string theory. Although it does not satisfy that requirement, it is similar to those that do. In string theory, when compactifying a higher-dimensional model into lower dimenions, additional degrees of freedom can be generated. For example, isometries of the internal manifold that is compactified translate into gauge fields in the resulting lower-dimensional theory [10]. This occurs when compactifying an 11-dimensional theory into four dimensions, which generates four $U(1)$ gauge fields similar to those in the first model studied in [4]. Although the model is not embedded in string theory, it captures many important properties of wormholes while remaining analytically and computationally tractable. Marolf and Santos identified a wormhole solution in this model that is free of negative modes, demonstrating that it dominates over the disconnected solution in certain regimes in a manner analogous to the Page transition in the entropy discussed above.

In general, when analyzing the stability of a wormhole solution, it is necessary to consider all the ways the mode can decay, including non-perturbative decay channels. One
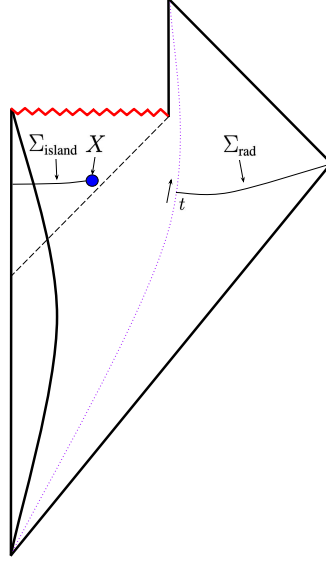
Figure 6. To compute the radiation entropy, the area of the surface X is added to the semiclassical entropy over the union between regions both outside and inside the black hole. This figure is adapted from [6].
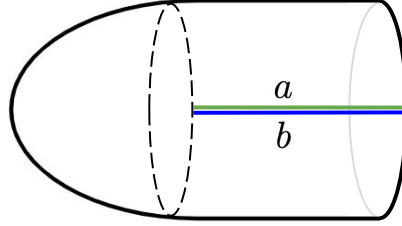

Figure 7. A schematic representation of the density matrix element ρ_{ab} of the black hole radiation. The states a and b correspond to exterior geometries that are glued together. This figure is adapted from [6].

way a wormhole saddle can decay non-perturbatively is brane nucleation, a phenomenon that occurs in string theory when a true vacuum corresponding to a brane solution has lower energy than the wormhole, as shown in Figure 9. Because the wormhole is a local minimum, it is perturbatively stable, but quantum fluctuations can produce a bubble of true vacuum that causes the wormhole solution to tunnel to the lower-energy state. Since the $U(1)^3$ model is an ad-hoc low-energy model, it does not contain branes that can lead to these brane-nucleation instabilities, but in a more general setting, these types of decay channels need to be considered.

The goal of this report is to review and reproduce the results of the Euclidean $U(1)^3$ model of Marolf and Santos, elaborating on the calculations and at times supplying original derivations. Although the model is relatively simple, the perturbative analysis required to determine negative modes does not simply involve diagonalization of a matrix, although this can be computationally intensive when the size of the matrix is large. Instead, because the background is not flat, there is a radial profile that leads to a dif-

$$\text{Tr}(\rho^2) \approx \quad + \quad + \cdots$$

Figure 8. The purity is computed using replicas of the geometry that can be connected in different ways, including connecting the interiors with a wormhole. This figure is adapted from [6].
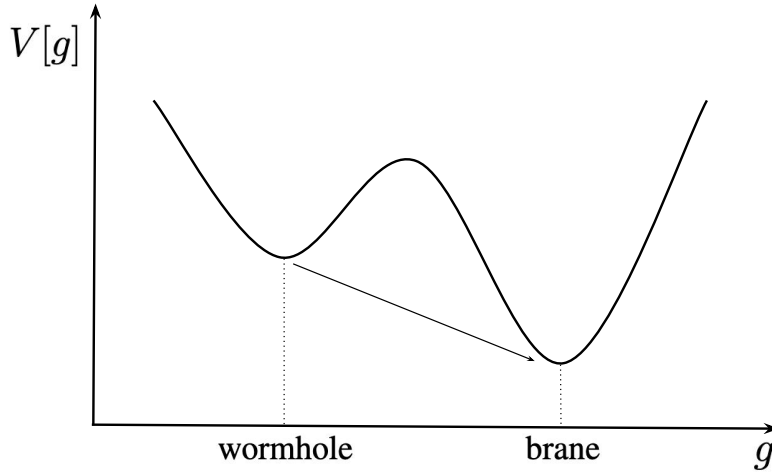

Figure 9. A false vacuum corresponding to a wormhole can tunnel through quantum fluctuations into a true vacuum corresponding to a brane solution. In this case, the wormhole is globally unstable even though it is perturbatively stable.

ferential equation that must be solved numerically. Different programs involving several symbolic and numerical tools were written to compute the various tensors, expand the action to second order, and solve the negative mode equation. The results are summarized in this report, but the same kind of analysis and programs can be applied to many different models.

2. Einstein-Maxwell Theory with an S^3 Boundary

The model consists of three Maxwell fields $F^i_{\mu\nu} = dA^i$ in four-dimensional AdS. After introducing the model, Section 2.1 discusses disconnected solutions, and Section 2.2 investigates connected, or wormhole, solutions. Scalar perturbations of the metric around the wormhole solution are discussed in Section 2.3, leading to the eigenvalue problem of Section 2.4 that can be searched for negative modes.

The action is given by

$$S = -\int_{\mathcal{M}} d^4x \sqrt{g} \left(R + \frac{6}{L^2} - \sum_{i=1}^{3} F^i_{\mu\nu} F_i^{\mu\nu} \right) - 2 \int_{\partial\mathcal{M}} d^3x \sqrt{h} K + \mathcal{S}_{\mathcal{B}}, \qquad (2)$$

8

where L is the AdS length scale, h is the determinant of the induced metric on the boundary $\partial\mathcal{M}$, and K is the extrinsic curvature associated with an outward-pointing normal to the boundary. The first integral is called the on-shell Euclidean action. The second term is the Gibbons-Hawking-York term needed to make the variational problem well-defined in the presence of a boundary. The final term, required to make the on-shell action finite, is given by

$$\mathcal{S}_\mathcal{B} = \int_{\partial\mathcal{M}} d^3x \sqrt{h} \left(\frac{4}{L} + L\mathcal{R} \right),$$

where $\mathcal{R}$ is the intrinsic Ricci scalar on $\partial\mathcal{M}$.

The equations of motion derived by varying Equation 2 with respect to the metric and fields are

$$R_{\mu\nu} + \frac{3}{L^2}g_{\mu\nu} = 2\sum_{i=1}^{3} \left(F^i_{\mu\rho}F^{i,\rho}_\nu - \frac{g_{\mu\nu}}{4}F^i_{\rho\sigma}F^{\rho\sigma}_i \right),$$
$$\nabla_\mu F^{\mu\nu}_i = 0.$$

The first equation is the trace-reversed Einstein equation, where the right-hand side is the energy-momentum of the Maxwell fields. The second equation represents the covariant Maxwell equations.

To find solutions to the equations, a spherically symmetric metric is used. The metric on the round three-sphere is

$$d\Omega^2 = \frac{1}{4}(\sigma_1^2 + \sigma_2^2 + \sigma_3^2),$$

where σ_i, expressed in terms of Euler angles, are

$$\sigma_1 = -\sin\psi\,d\theta + \cos\psi\sin\theta\,d\varphi,$$
$$\sigma_2 = \cos\psi\,d\theta + \sin\psi\sin\theta\,d\varphi,$$
$$\sigma_3 = d\psi + \cos\theta\,d\varphi,$$

with $\psi \in (0, 4\pi)$, $\theta \in (0, \pi)$, and $\varphi \in (0, 2\pi)$. The four-dimensional metric takes the form

$$ds^2 = \frac{dr^2}{f(r)} + g(r)d\Omega^2,$$

with $r \in (0, \infty)$, where $r = \infty$ corresponds to the conformal boundary. The vector potentials are given by

$$A^i = L\frac{\sigma_i}{2}\Phi(r).$$

Both disconnected and connected, or wormhole, solutions can be constructed from the metric by appropriate choice of the function g, which represents the gauge freedom of the metric.

2.1. Disconnected Solutions

To find disconnected solutions, the choice $g(r) = r^2$ is made. At $r = 0$, the round three-sphere smoothly shrinks to zero. With this choice, the metric becomes

$$g_{\mu\nu} = \begin{pmatrix} \frac{1}{f(r)} & 0 & 0 & 0 \\ 0 & \frac{1}{4}r^2 & 0 & \frac{1}{4}r^2\cos\theta \\ 0 & 0 & \frac{1}{4}r^2 & 0 \\ 0 & \frac{1}{4}r^2\cos\theta & 0 & \frac{1}{4}r^2 \end{pmatrix}.$$

The distinct Einstein equations are

$$2r^4 - L^2 r^3 f'(r) = 2L^4\left[r^2 f(r)\Phi'(r)^2 - 4\Phi(r)^2\right], \tag{3}$$

$$6r^4 - L^2 r^2\left[rf'(r) + 4f(r) - 4\right] = 2L^4\left[4\Phi(r)^2 - r^2 f(r)\Phi'(r)^2\right]. \tag{4}$$

The Maxwell equations reduce to

$$2r^2 f(r)\Phi''(r) + r^2\Phi'(r)f'(r) + 2rf(r)\Phi'(r) - 8\Phi(r) = 0. \tag{5}$$

Regularity of the metric and fields requires

$$f(0) = 1,$$
$$\Phi'(r) = 0.$$

With those boundary conditions, the solutions to Equations 3–5 are

$$f(r) = 1 + \frac{r^2}{L^2},$$
$$\Phi(r) = \Phi_0 \frac{\sqrt{L^2 + r^2} - L}{\sqrt{L^2 + r^2} + L}.$$

It turns out that the energy-momentum tensor is zero, and that the disconnected solutions are vacuum solutions. The on-shell Euclidean action of the solution evaluates to

$$S_D = 8\pi^2 L^2 \left(1 + 3\Phi_0^2\right). \tag{6}$$

2.2. Connected Solutions

Connected solutions exhibit a wormhole throat with a minimum radius r_0. To achieve this, the gauge can be set to $g(r) = r^2 + r_0^2$. There are two asymptotic regions, at $r = \pm\infty$. A global $\mathbb{Z}_2$ symmetry relates the two spheres while leaving the minimal sphere invariant.

With the new gauge choice, the unique Maxwell equation is

$$(r^2 + r_0^2)\left[2f(r)\Phi''(r) + f'(r)\Phi'(r)\right] + 2rf(r)\Phi'(r) - 8\Phi(r) = 0,$$

which simplifies to

$$\frac{d}{dr}\left[(r^2 + r_0^2)f(r)\Phi'(r)^2 - 4\Phi(r)^2\right] = 0.$$

After integration, this becomes

$$f(r) = \frac{C + 4\Phi(r)^2}{(r^2 + r_0^2)\Phi'(r)^2}, \tag{7}$$

where C is the constant of integration. Using Equation 7, the Einstein equations are

$$2\left(r^2 + r_0^2\right)^2 - L^2\left[(r^2 + r_0^2)rf'(r) + 2r_0^2 f(r)\right] = 2CL^4,$$

$$6\left(r^2 + r_0^2\right)^2 - L^2\left[(r^2 + r_0^2)(rf'(r) + 2f(r) - 4) + 2r^2 f(r)\right] = -2CL^4.$$

Combining these two equations yields

$$\Phi'(r)^2 - \frac{L^2 r^2[C + 4\Phi(r)^2]}{(r^2 + r_0^2)\left[CL^4 + (r^2 + r_0^2)(L^2 + r^2 + r_0^2)\right]} = 0. \tag{8}$$

Rearranging, and again using Equation 7, results in

$$f(r) = \frac{CL^4 + (r^2 + r_0^2)(L^2 + r^2 + r_0^2)}{L^2 r^2}. \tag{9}$$

To avoid a singularity at $r = 0$, the integration constant must be

$$C = -\frac{L^2 r_0^2 + r_0^4}{L^4}.$$

With this choice, Equation 9 becomes

$$f(r) = \frac{L^2 + r^2 + 2r_0^2}{L^2}.$$

From Equation 8, it can be shown that the solution for Φ is

$$\Phi(r) = \Phi_* \cosh\left[\frac{2}{b}F\left(\arctan\left(\frac{r}{La}\right)\middle| 1 - \frac{a^2}{b^2}\right)\right], \tag{10}$$

where $a \equiv (1 + 16\Phi_*^2)^{1/4}$ and $b \equiv r_0/L$. The function $F(\phi|m)$ is the elliptic integral of the first kind. The elliptic integral parameters are related by

$$b = \sqrt{\frac{a^2 - 1}{2}}.$$

Figure 10 is a plot of $\Phi(r)$ for $\Phi_* = 2$ and $L = 1$. For some background on elliptic integrals, see Appendix A.2.

The source of the Maxwell fields corresponds to $\Phi(r)$ at $r = \infty$. Taking the $r = \infty$ limit of Equation 10, the argument of the elliptic integral becomes $\pi/2$, reducing it to the complete elliptic integral of the first kind, $K(m)$. The source Φ_0 as a function of Φ_* is then

$$\Phi_0(\Phi_*) = \Phi_* \cosh\left[\frac{2}{b}K\left(1 - \frac{a^2}{b^2}\right)\right]. \tag{11}$$
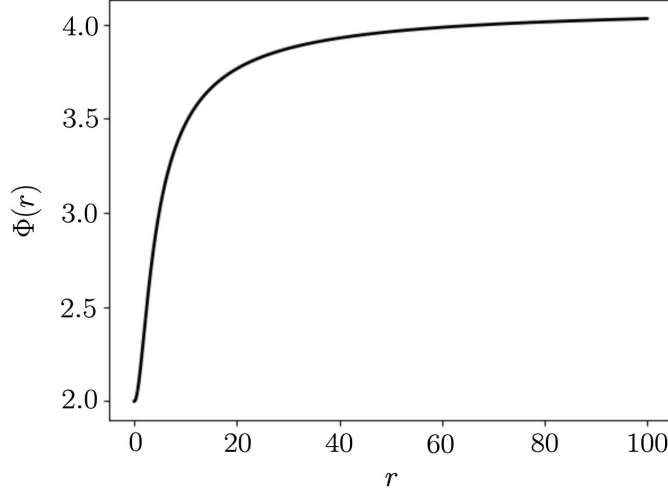
11

Figure 10. Plot of the Maxwell field solution $\Phi(r)$ involving the hyperbolic cosine of the elliptic integral of the first kind. The parameters $\Phi_* = 2$ and $L = 1$ were used.

For a single value of the source Φ_0, there can be two values of Φ_*, as shown in Figure 11. Wormhole solutions only exist if $\Phi_0 \geq \Phi_0^{\min} \approx 3.5633$, which corresponds to $\Phi_* = \Phi_*^{\min} \approx 1.0023$. The different values of Φ_* correspond to different wormhole solutions.

Another way of analyzing the two wormhole solutions is by studying how the radius of the wormhole throat changes with the source, as depicted in Figure 12. For Φ_0 above the minimum, there are two values of r_0, which correspond to small and large wormholes. At $r_0^{\min} \approx 1.2515L$, the two wormholes merge. It turns out that only the small wormhole exhibits a negative mode.

Substituting the connected wormhole solution into the on-shell Euclidean action of Equation 2, and evaluating the integral, leads to the action

$$S_C = \frac{8\pi^2 L^2}{(X-1)^{3/2}} \left[2(X-1)E(-X) - (X-2)K(-X) + \tag{12} \right.$$

$$\left. \frac{3X}{4\sqrt{X-1}} \sinh\left(4\sqrt{X-1}K(-X)\right) \right],$$

where $X \equiv 1 + L^2/r_0^2$ and $E(m)$ is the complete elliptic integral of the second kind. To assess whether the connected solution has a lower action than the disconnected one, Equation 12 can be subtracted from Equation 6 to produce the metric

$$\Delta S \equiv 2S_D - S_C,$$

which is plotted in Figure 13. The upper and lower branches correspond to the large and small wormhole, respectively. If $\Delta S > 0$, the wormhole solution has a lower action, so it should dominate in the path integral. The large wormhole is dominant for $\Phi_0 \gtrsim 3.8597$, while the small wormhole is always subdominant. The transition in dominance between the disconnected and large wormhole solutions is analogous to the transition between disconnected and wormhole saddles during black hole evaporation.
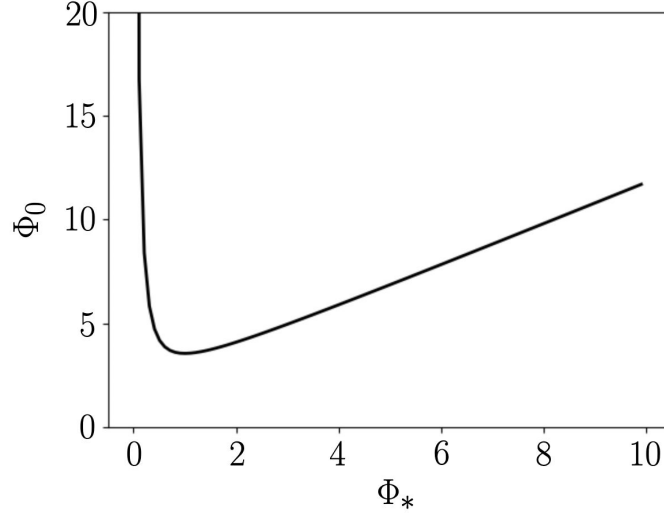
Figure 11. The source of the Maxwell fields Φ_0 as a function of Φ_*. There are two types of wormhole solutions for each value of Φ_0 above the minimum, Φ_0^{min}.

2.3. Scalar Perturbations

To identify negative modes, the metric can be perturbed around the wormhole solution. There are several types of perturbations, including scalar, vector, and tensor perturbations, but this report will only focus on scalar perturbations. The metric and fields take the same form as before, with perturbations δg, δf, and $\delta \Phi$ applied to the background fields as

$$g(r) = \overline{g}(r) + \delta g(r),$$
$$f(r) = \overline{f}(r) + \delta f(r),$$
$$\Phi(r) = \overline{\Phi}(r) + \delta \Phi(r),$$

where $\overline{\Phi}(r)$ is given by Equation 10 and

$$\overline{g}(r) = r^2 + r_0^2,$$
$$\overline{f}(r) = \frac{L^2 + r^2 + 2r_0^2}{L^2}.$$

The action is expanded to second order in the perturbations. Integrating out the angular part, the Euclidean on-shell action is

$$S_E = \frac{\pi^2}{8L^2} \int \frac{dr}{\sqrt{fg}} \left[12L^4 \left(4\Phi^2 + fg\Phi'^2 \right) + 3L^2 \left(2fg'' + f'g' - 4 \right) - 12g^2 \right],$$

where, for simplicity, the explicit dependence on r in the various functions has been
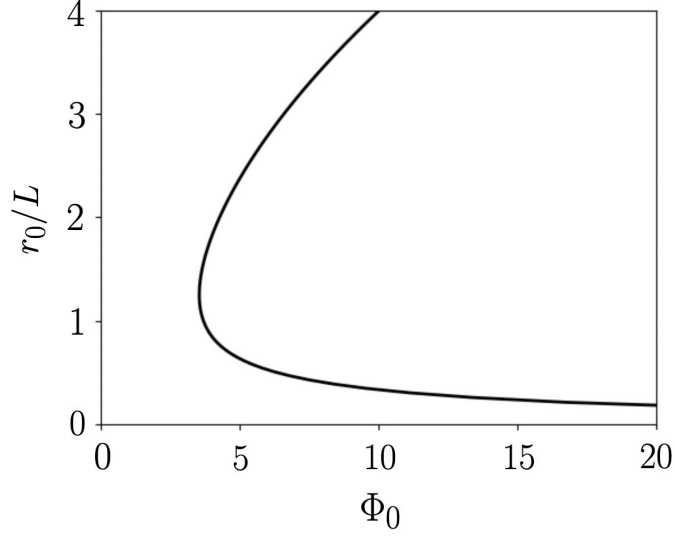
13

Figure 12. The radius of the wormhole throat r_0/L as a function of Φ_0. For $\Phi_0 \geq \Phi_0^{\min}$, small and large wormholes exist.

removed. The variations with respect to δg and δf

$$
\frac{\delta S_E}{\delta g} = -\frac{3\pi^2}{16L^2} \int \frac{dr}{\sqrt{fg^3}} \left[12g^2 + 16L^4\Phi^2 + L^2 fg'^2 - \right.
$$
$$
\left. 2L^2 g\left(2fg'' + 2fL^2\Phi'^2 + f'g' - 2\right)\right],
$$
$$
\frac{\delta S_E}{\delta f} = \frac{3\pi^2}{16L^2} \int \frac{dr}{\sqrt{gf^3}} \left[4g^2 - 16L^4\Phi^2 - L^2 fg'^2 + 4g\left(L^2 + L^4 f\Phi'^2\right)\right]
$$

vanish because of the Einstein equations. The variation with respect to $\delta\Phi$ also vanishes because of the unique Maxwell equation

$$
\frac{\delta S_E}{\delta\Phi} = -\frac{3L^2\pi^2}{2} \int \frac{dr}{\sqrt{fg}} \left(fg'\Phi' + gf'\Phi' + 2fg\Phi'' - 8\Phi \right).
$$

The second-order variation of the action can be decomposed into a part dependent on δg and $\delta\Phi$ and their derivatives, and a part dependent on δf and its derivative. After integration by parts, the second part has no reliance on $\delta f'$. Using Equation 7, the f component of the second-order action is

$$
S_f^{(2)} = \frac{\pi^2}{32L^2} \int \frac{dr}{(\overline{g}\overline{f})^{3/2}} \left[12L^2\overline{g}\left(L^2\overline{g}\overline{\Phi}'^2 - 3r^2\right)\delta f^2 - 192L^4\overline{g}\overline{\Phi}\delta f\delta\Phi + \right.
$$
$$
48L^4\overline{f}\overline{g}^2\overline{\Phi}'\delta f\delta\Phi' + 12L^2\overline{g}\overline{f}\overline{g}'\delta f\delta g' -
$$
$$
\left. 3\left(16L^4\overline{\Phi}^2 + 4L^4\overline{f}\overline{g}\overline{\Phi}'^2 + L^2\overline{f}\overline{g}'^2 + 4L^2\overline{g} + 12\overline{g}^2\right)\delta f\delta g\right].
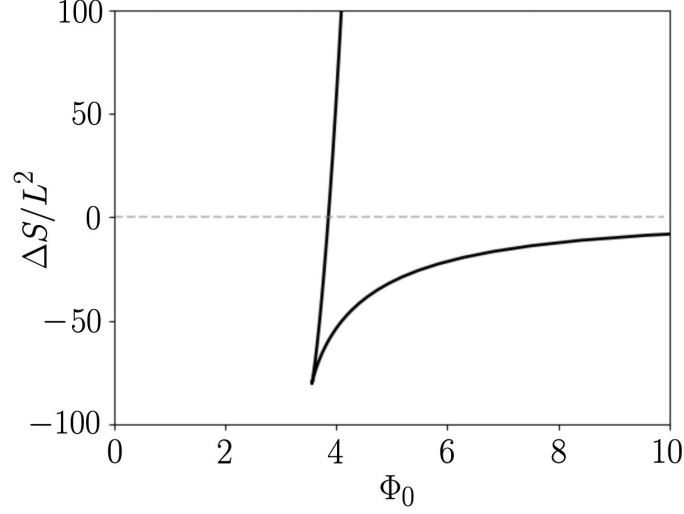$$

14

Figure 13. The difference in the on-shell Euclidean action between the disconnected and connected wormhole solutions. The upper branch corresponds to the large wormhole, which becomes dominant when $\Delta S > 0$, meaning the connected solution has a lower action.

This action is invariant under the infinestimal gauge transformation $\xi \equiv \xi_r(r)\partial_r$. Under this transformation, a metric perturbation h and gauge field a transform as

$$\Delta h = \mathcal{L}_\xi \overline{g},$$
$$\Delta a = \mathcal{L}_\xi \overline{A},$$

where $\mathcal{L}_\xi$ is the Lie derivative along ξ, and $(\overline{g}, \overline{A})$ are the metric and gauge potential background fields. Notice the $\overline{g}$ here is different than the $\overline{g}$ above. From the definition of the Lie derivative, the perturbations transform as

$$\Delta \delta f = \xi_r \overline{f}' - 2\overline{f}\xi_r', \tag{13}$$
$$\Delta \delta g = 2r\xi_r, \tag{14}$$
$$\Delta \delta \Phi = \xi_r \overline{\Phi}'. \tag{15}$$

The transformations of the perturbation derivatives are

$$\Delta \delta g' = 2\xi_r + 2r\xi_r',$$
$$\Delta \delta \Phi' = \xi_r \overline{\Phi}'' + \xi_r' \overline{\Phi}'.$$

Using these transformations, it follows that the gauge transformation of the action, $\Delta S_f^{(2)}$, is zero. Since the action is gauge invariant, it is convenient to choose $\delta g = 0$. The action simplifies to

$$S_f^{(2)} = \frac{3\pi^2}{8} \int \frac{dr}{\sqrt{\overline{f}\overline{g}^3}} \left[\left(L^2 \overline{g}\overline{\Phi}'^2 - 3r^2 \right)\delta f^2 - L^2 \overline{\Phi}\delta f \delta \Phi + 4L^2 \overline{g}^2 \overline{\Phi}' \delta f \delta \Phi' \right].$$

Given the algebraic dependence on δf in the action, the square can be completed, transforming the action into the form

$$S_f^{(2)} = \int dr \left[-\left(a_1 \delta f + a_2 \delta \Phi + a_3 \delta \Phi' \right)^2 + C_0 \right],$$

15

where a_i are functions of the background fields only. The first term is a Gaussian integral that can be computed, and the result can be absorbed into the measure in the path integral. The remaining part involving C_0 is given by

$$S_f^{(2)} = \frac{\pi^2}{2} \int \frac{dr}{\sqrt{\overline{g}\overline{f}^3}\left(r^2 - L^2\overline{g}\overline{\Phi}'^2\right)} \Bigg[48L^4\overline{\Phi}^2\delta\Phi^2 + 24L^4\overline{f}\overline{g}\overline{\Phi}\,\overline{\Phi}'\delta\Phi\delta\Phi' +$$
$$3L^4\left(\overline{f}\overline{g}\overline{\Phi}'\right)^2\delta\Phi'^2 \Bigg].$$

The part of the action not involving f can be expressed in terms of the gauge invariant quantity

$$q \equiv \delta\Phi - \overline{\Phi}'\frac{\delta g}{2r}.$$

Using Equations 13–15, it can be shown that $\Delta q = 0$. When $\delta g = 0$, $q = \delta\Phi$. Making that simplification, the q part of the action is

$$S_q^{(2)} = \frac{3L^2\pi^2}{2} \int \frac{dr}{\sqrt{\overline{g}\overline{f}}} \left(4q^2 + \overline{f}\overline{g}q'^2 \right).$$

The two parts of the action can be combined. After performing integration by parts on the qq' term, the result is

$$S^{(2)} = \frac{\pi^2}{4} \int dr \sqrt{\frac{\overline{g}}{\overline{f}}} \left(\overline{f}Kq'^2 + Vq^2 \right), \tag{16}$$

where

$$K \equiv \frac{6L^2r^2}{r^2 - L^2\overline{g}\overline{\Phi}'^2},$$

$$V \equiv \frac{4K}{\overline{g}} \left[\frac{2\overline{g}}{L^2r\overline{f}} \frac{L^2\left(r - L^2\overline{\Phi}\,\overline{\Phi}'\right) + \overline{g}\left(r - 2L^2\overline{\Phi}\,\overline{\Phi}'\right)}{r^2 - L^2\overline{g}\overline{\Phi}'^2} - 1 \right].$$

2.4. Negative Modes

To search for negative modes, the first term in Equation 16 needs to be integrated by parts, resulting in

$$S^{(2)} = \frac{\pi^2}{4} \int dr \sqrt{\frac{\overline{g}}{\overline{f}}} q \left[-\sqrt{\frac{\overline{f}}{\overline{g}}}\left(\sqrt{\overline{f}\,\overline{g}}Kq'\right)' + Vq \right].$$

The negative mode equation is then

$$-\sqrt{\frac{\overline{f}}{\overline{g}}}\left(\sqrt{\overline{f}\,\overline{g}}Kq'\right)' + Vq = \lambda q. \tag{17}$$

If this admits non-trivial solutions for $\lambda < 0$, the wormhole solution is locally unstable. Since $V(r)$ is symmetric around $r = 0$, modes can be decomposed into ones where

$q(0) = 0$, and others where $q'(0) = 0$. Equation 17 can be solved numerically given these boundary conditions. Since r has an infinite range, it is convenient for numerical calculations to switch to a variable with a finite range, introducing

$$r = \frac{r_0 y}{1 - y},$$

so that the conformal boundary lies at $y = 1$ and the origin at $y = 0$. Expanding the derivative in Equation 17 and changing variables, the negative mode equation becomes

$$-K\overline{f}\frac{d^2 y}{dr^2}q''(y) - \left(\overline{f}\frac{dK}{dr} + \frac{rK\overline{f}}{\overline{g}} + \frac{rK}{L^2}\right)\frac{dy}{dr}q'(y) + V(r)q(y) = \lambda q(y). \qquad (18)$$

The negative mode equation can be solved numerically by discretizing it and solving the resulting matrix equation using different methods, including QZ factorization and Newton-Raphson search [11; 12]. Discretization involves choosing points on the domain, and approximating the derivatives at those points using an interpolation function. This reduces differentiation to a matrix operation

$$q'_i \approx D_{ij}q_j.$$

There are several discretization schemes that differ in their choice of grid and interpolation function. The Chebyshev method is a popular method that reduces potentially large oscillations in the interpolated function by sampling points more densely near the edges. This method was used to sample 50 points along the y axis from 0 to 0.99, which excludes the singularity at $y = 1$. See Appendix A.3 for an evaluation of the numerical accuracy.

After discretization, Equation 18 takes the form $A_{ij}q_j = \lambda B q_i$, which is the form of the generalized eigenvalue problem that can be solved using matrix factorization. To incorporate the boundary conditions, the last rows of A and B can be modified to reproduce the corresponding equations, either $q(0) = 0$ or $q'(0) = 0$. In both cases, this involves replacing the last row of B with zeros, since the boundary conditions do not involve λ. For $q(0) = 0$, the last row of A should be one at $y = 0$ and zero otherwise. For $q'(0) = 0$, the last row must be replaced by the row of D_{ij} corresponding to $y = 0$.

To determine whether the small or large wormholes exhibit negative modes, the eigenvalue problem can be solved for different values of the wormhole throat, r_0. Since $\Phi(r)$ depends on r_0 through b, adjusting r_0 results in different A matrices and different eigenvalues. Table 1 summarizes the results for the case $q'(0) = 0$. When r_0 is less than $r_0^{\min}$, which corresponds to the small wormhole, there is one negative mode. As the wormhole becomes large, the negative mode disappears. Due to the numerical instability of the problem, these results were sensitive to the matrix entries, but the general trend of negative modes for the small wormhole, and positive modes for the large wormhole, was observed. When $q(0) = 0$, no negative modes were detected for any value of r_0.

3. Conclusion

Wormholes are important solutions to general relativity that connect asymptotic regions of spacetime. There are many different types of wormhole solutions, but they are generally classified as Lorentzian or Euclidean, depending on the signature of the metric.

$r_0/r_0^{\mathbf{min}}$	Eigenvalues
0.8	One negative eigenvalue, $\lambda = -118$
1.0	No negative eigenvalues, $\lambda_{\min} = 1.92 \times 10^{-7}$
1.1	No negative eigenvalues, $\lambda_{\min} = 1.41 \times 10^{-6}$

Table 1. The eigenvalues of the second-order action around the wormhole solution when $q'(0) = 0$. There is one negative mode when the wormhole throat is less than $r_0^{\mathbf{min}}$, which becomes positive when $r_0^{\mathbf{min}}$ is exceeded.

While Lorentzian wormholes may physically connect different parts of the universe, Euclidean wormholes primarily emerge as saddles of the Euclidean gravitational path integral. While these types of wormholes have been studied for decades, they have received renewed interest because they challenge the traditional understanding of the AdS/CFT correspondence and because of their role in resolving the black hole information paradox. Many different types of Euclidean wormholes have been identified, but they only make significant contributions to the underlying physics if they do not contain negative modes. This report focused on examining wormhole solutions and their negative modes.

Following [4], it was shown that a gravitational theory containing three Maxwell fields has small and large wormhole solutions. The large wormhole solution has a lower Euclidean action than the disconnected one when the source of the Maxwell fields exceeds a critical value. The transition between the disconnected solution and the wormhole mimics the phase transition witnessed between the disconnected and wormhole saddles when computing the entropy of black hole radiation. By conducting a perturbative analysis around the wormhole solution and solving the resulting eigenvalue problem numerically, both negative and positive modes were detected, but the large wormhole did not exhibit negative modes. This indicates that, at least in this simple model, the large wormhole may dominate the path integral, violating factorizability and suggesting that there may be correlations in the dual quantum field theories on the boundaries.

While the model investigated here is illuminating, no definitive conclusions about the AdS/CFT correspondence can be based on it. This is because the AdS/CFT correspondence is a relation involving string theories, but the current model does not embed directly into string theory. For models based on string and M-theory compactifications, non-perturbative decay channels like brane-nucleation instabilities need to be considered. Marolf and Santos showed that wormholes in these models that are large enough to dominate over disconnected solutions always suffer from these instabilities. They also identified wormholes that are free of both perturbative and non-perturbative instabilities, but they do not dominate over disconnected solutions.

While subdominant wormholes do not control leading-order effects, they are still important for computing quantities like $\delta Z^2 \equiv \langle Z^2 \rangle - \langle Z \rangle^2$ that measure the loss of factorizability in the path integral. This is because the contribution of disconnected solutions to this quantity is zero. Unless some mechanism exists that drives δZ^2 to zero, even subdominant saddles will make it take on a non-zero value. As [4] concluded, this means that the factorization problem of AdS/CFT is far from resolved and will be the subject of much future research.

A. Appendix

A.1. Code

While the model examined in this report is relatively simple and for the most part analytically tractable, conducting all the calculations by hand is very time-consuming, error-prone, and does not extend easily to other models. The second-order negative mode equation involving complicated functions of the radial coordinate also needs to be solved numerically. In this way, programmatic ways of manipulating symbolic equations and solving them numerically need to be relied on. One major contribution of this report was the creation of Python and Mathematica programs to perform the extensive calculations needed to identify and study wormhole solutions in physically interesting settings.

Several packages were used to produce the results. In Python, `sympy` was used for symbolic computation, including tensor algebra [13]. This package essentially functions as a computer algebra system similar to languages like Mathematica. Calculations of the Ricci tensor and scalar were performed using `einsteinpy` [14]. Jupyter notebooks were used to run and analyze the results [15]. Mathematica was relied on primarily for computing variational derivatives of the action using `VariationalMethods`, which Python cannot do easily. The code can be found in [16]. The relevant notebooks include

- `einstein_maxwell_ads4_euclidean`. Calculates all the quantities in the Einsten and Maxwell equations and verifies the disconnected solution
- `einstein_maxwell_ads4_euclidean_connected`. Verifies the connected wormhole solution
- `einstein_maxwell_ads4_scalar_perturb`. Calculates the variation of the on-shell action
- `second_order_action_analysis`. Calculates the form of the second-order action
- `gauge_invariance_action`. Demonstrates the gauge invariance of the second-order action
- `negative_modes_analysis`. Demonstrates the negative modes for the small wormhole and lack of negative modes for the large wormhole
- `perturbations`. Calculates the first-order variational derivatives of the action to corroborate calculation of the second-order action elsewhere

The remainder of this section provides code snippets that perform some common calculations using the various packages.

A.1.1. General Relativity Calculations

Listing 1 is an example of computing tensors needed in general relativity. After defining the required symbolic variables using `sympy` on lines 6–10, the metric is defined on lines 13–18. In this example, the disconnected form of the metric is used, but the connected metric can be defined the same way. On lines 21–25, the Ricci and Einstein tensors are calculated.

```
1 # import packages
2 import sympy
3 from einsteinpy.symbolic import RicciTensor, RicciScalar, MetricTensor,
      ChristoffelSymbols
```

19

```
4
5  # define variables
6  syms = sympy.symbols("r psi theta phi")
7  r, psi, theta, phi = syms
8  f = sympy.Function('f')(r)   # metric ansatz
9  L = sympy.symbols("L")   # AdS length scale
10 cap_phi = sympy.Function('Phi')(r)   # defines gauge field
11
12 # define metric tensor
13 list2d = [[0 for i in range(4)] for i in range(4)]
14 list2d[0][0] = 1 / f
15 list2d[1][1] = list2d[2][2] = list2d[3][3] = r ** 2 / 4
16 list2d[1][3] = list2d[3][1] = r ** 2 / 4 * sympy.cos(theta)
17 sch = MetricTensor(list2d, syms)
18 metric_array = sympy.MutableDenseNDimArray(list2d)
19
20 # compute Ricci tensor
21 Ric = RicciTensor.from_metric(sch)
22
23 # calculate Einstein tensor
24 einstein_tensor = sympy.MutableDenseNDimArray(Ric.tensor()) + 3 / L **
      2 * metric_array
25 einstein_tensor = sympy.simplify(einstein_tensor)
```

Listing 1. Example of computing the Ricci and Einstein tensors symbolically using `einsteinpy`.

A.1.2. Tensor Algebra Calculations

Often in general relativity calculations, it is necessary to contract tensor indices. Listing 2 is an example of computing the energy-momentum tensor of a Maxwell field, which involves various contractions. Note that this example is not self-contained, but uses some variables defined in Listing 1. After defining the vector potential on line 5, lines 8–17 compute the field strength tensor. Using `sympy`, lines 20–26 compute the first term in the energy-momentum tensor involving a single contraction. The object `TensorHead` is used to perform the contraction. Lines 29–32 do the same for the second term, and the final result is computed on line 35.

```
1  # import packages
2  from sympy.tensor.tensor import TensorIndexType, TensorIndex,
      TensorHead, tensor_indices, TensorSymmetry
3
4  # define vector potential
5  A = L / 2 * cap_phi * sympy.Array([0, 0, -sympy.sin(psi), sympy.cos(psi
      ) * sympy.sin(theta)])
6
7  # compute field strength tensors
8  x = [r, psi, theta, phi]
9  def em_field_strength(A):
10     """Compute EM field strength from the vector potential."""
11     F = sympy.MutableDenseNDimArray.zeros(4, 4)
12     for i in range(4):
13         for j in range(4):
14             F[i, j] = sympy.diff(A[j], x[i]) - sympy.diff(A[i], x[j])
```

```
15      return F
16
17  F = em_field_strength(A)
18
19  # compute first term of energy-momentum tensor involving single
        contraction
20  metric_inv = sympy.Matrix(metric_array).inv()
21  Euclidean = TensorIndexType('Euclidean', dummy_name='E')
22  i0, i1, i2, i3, i4, i5, i6, i7 = tensor_indices('i0:8', Euclidean)
23  FFg_tensor = TensorHead('FFg', [Euclidean] * 6)
24  FFg_matrix = sympy.tensorproduct(F, F, metric_inv)
25  repl = {FFg_tensor(-i0, -i1, -i2, -i3, i4, i5): FFg_matrix}
26  T_contracted_1 = FFg_tensor(-i0, -i1, -i2, -i3, i3, i1).
        replace_with_arrays(repl)
27
28  # compute second term of energy-momentum tensor involving two
        contractions
29  FFgg_tensor = TensorHead('FFgg', [Euclidean] * 8)
30  FFgg_matrix = sympy.tensorproduct(F, F, metric_inv, metric_inv)
31  repl = {FFgg_tensor(-i0, -i1, -i2, -i3, i4, i5, i6, i7): FFgg_matrix}
32  T_contracted_2 = FFgg_tensor(-i0, -i1, -i2, -i3, i3, i1, i2, i0).
        replace_with_arrays(repl)
33
34  # compute energy-momentum tensor
35  energy_momentum = 2 * (T_contracted_1 - metric_array / 4 *
        T_contracted_2)
```

Listing 2. Example of calculating the energy-momentum tensor of a Maxwell field using `sympy`.

A.2. Elliptic Integrals

Elliptic integrals historically arose in the context of finding the arc length of an ellipse [17]. They can be applied to many areas of physics, including determining the motion of a simple pendulum or the deflection of a thin elastic bar. An elliptic integral is an integral of the form

$$\int \frac{A(x) + B(x)}{C(x) + D(x)\sqrt{S(x)}} \, dx,$$

where A, B, C, and D are polynomials in x and S is a polynomial of degree three or four.

Elliptic integrals come in three different kinds. The incomplete elliptic integral of the first kind is given by

$$F(\phi|m) \equiv \int_0^\phi \frac{d\theta}{\sqrt{1 - m^2 \sin^2 \theta}}.$$

The parameter ϕ is called the amplitude, and m the modulus. The complete integral integral of the first kind is obtained by setting $\phi = \pi/2$, $K(m) \equiv F(\pi/2, m)$. The incomplete elliptic integral of the second kind is given by

$$E(\phi|m) \equiv \int_0^\phi \sqrt{1 - m^2 \sin^2 \theta} \, d\theta.$$

As before, the complete version is $E(m) \equiv E(\pi/2, m)$. The third kind is written similarly to the first two, but it is not used in this report and will not be reviewed.

21

A.3. Chebyshev Differentiation

To solve a differential equation numerically, the function and its derivatives need to be discretized. There are different ways of choosing discretization points and interpolating between them to approximate the derivatives. One of the simplest discretization methods is finite differencing. An example of this method is second-order central differencing, which produces the first and second derivatives at the discretization points

$$f_i' = \frac{f_{i+1} - f_{i-1}}{2\Delta x},$$
$$f_i'' = \frac{f_{i+1} - 2f_i + f_{i-1}}{\Delta x^2},$$

where Δx is the spacing between the points. Another popular method is Chebyshev differentiation. By using unevenly spaced points, it mitigates potentially large errors that occur near the edges of the domain. The discretization points are

$$x_i = \frac{1}{2}\left(x_{\min} + x_{\max}\right) + \frac{1}{2}\left(x_{\max} - x_{\min}\right)\cos\left(\frac{i\pi}{N}\right), \ i = 0, 1, \ldots, N,$$

where $x_{\min}$ and $x_{\max}$ define the minimum and maximum of the domain. The differentiation matrix is given by

$$D_{ij} = \begin{cases} \sum_{k \neq i} \frac{1}{x_i - x_k}, & i = j \\ \frac{a_i}{a_j(x_i - x_j)}, & i \neq j \end{cases}$$

where

$$a_i = \prod_{j \neq i}(x_i - x_j).$$

Figure 14 shows the result of applying Chebyshev differentiation to approximate the first and second derivatives of $u(x) = e^x \sin 5x$. The blue points are the estimated derivatives at the sampled points, while the black curves are the true derivatives. When $N = 10$ points are used, the estimates track the true values, but there can be large errors. With $N = 50$ points, the reconstruction error is very small. Notice that the functions are sampled more densely near the edges.
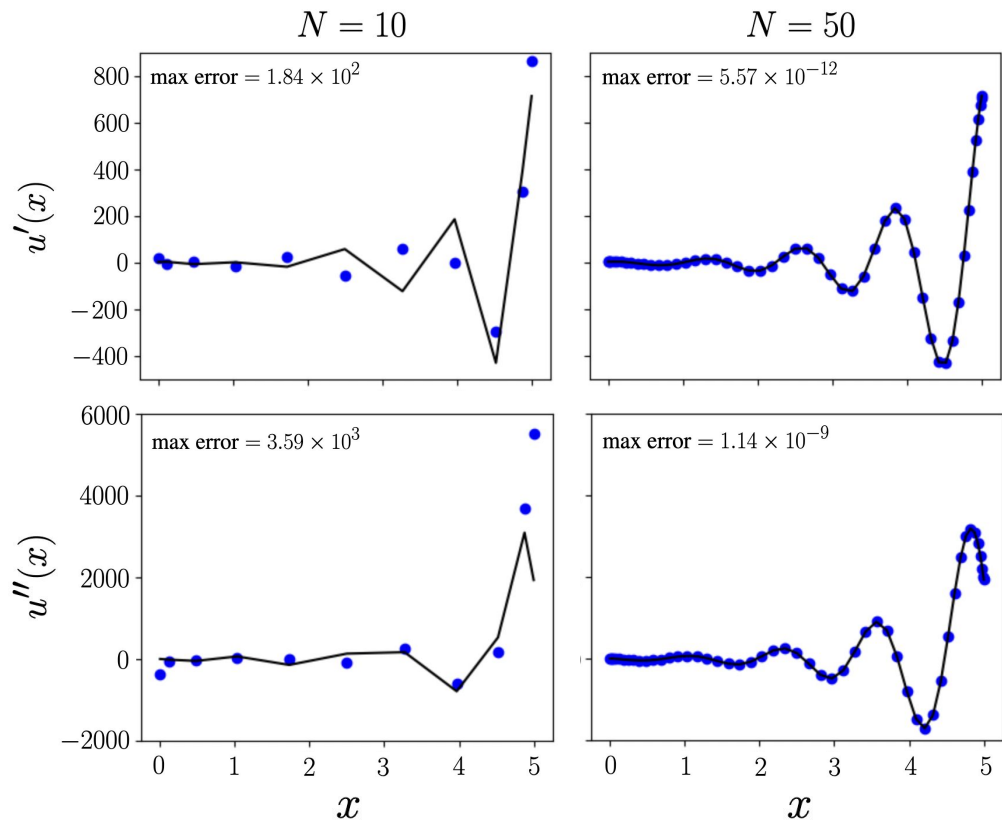
Figure 14. Chebyshev differentiation of $u(x) = e^x \sin 5x$ **using different amounts of discretization points. When** $N = 10$**, the estimation error of** u' **and** u'' **is large, but when** $N = 50$**, the error becomes very low.**

References

[1] A. Kundu, "Wormholes and Holography: An Introduction," *The European Physical Journal C*, vol. 82, no. 5, may 2022. [Online]. Available: https://doi.org/10.1140%2Fepjc%2Fs10052-022-10376-z

[2] J. Maldacena, "The Large N Limit of Superconformal Field Theories and Supergravity," *International Journal of Theoretical Physics*, vol. 38, no. 4, pp. 1113–1133, 1999. [Online]. Available: https://doi.org/10.1023%2Fa%3A1026654312961

[3] J. Maldacena and L. Maoz, "Wormholes in AdS," *Journal of High Energy Physics*, vol. 2004, no. 02, pp. 053–053, feb 2004. [Online]. Available: https://doi.org/10.1088%2F1126-6708%2F2004%2F02%2F053

[4] D. Marolf and J. E. Santos, "AdS Euclidean wormholes," *Classical and Quantum Gravity*, vol. 38, no. 22, p. 224002, oct 2021. [Online]. Available: https://doi.org/10.1088%2F1361-6382%2Fac2cb7

[5] D. N. Page, "Information in Black Hole Radiation," *Physical Review Letters*, vol. 71, no. 23, pp. 3743–3746, dec 1993. [Online]. Available: https://doi.org/10.1103%2Fphysrevlett.71.3743

[6] A. Almheiri, T. Hartman, J. Maldacena, E. Shaghoulian, and A. Tajdini, "The Entropy of Hawking Radiation," *Reviews of Modern Physics*, vol. 93, no. 3, jul 2021. [Online]. Available: https://doi.org/10.1103%2Frevmodphys.93.035002

[7] S. Ryu and T. Takayanagi, "Holographic Derivation of Entanglement Entropy from the anti–de Sitter Space/Conformal Field Theory Correspondence," *Physical Review Letters*, vol. 96, no. 18, may 2006. [Online]. Available: https://doi.org/10.1103%2Fphysrevlett.96.181602

[8] J. D. Bekenstein, "Black Holes and Entropy," *Phys. Rev. D*, vol. 7, pp. 2333–2346, Apr 1973. [Online]. Available: https://link.aps.org/doi/10.1103/PhysRevD.7.2333

[9] N. Engelhardt and A. C. Wall, "Quantum Extremal Surfaces: Holographic Entanglement Entropy beyond the Classical Regime," *Journal of High Energy Physics*, vol. 2015, no. 1, jan 2015. [Online]. Available: https://doi.org/10.1007%2Fjhep01%282015%29073

[10] K. Becker, M. Becker, and J. H. Schwarz, *String Theory and M-Theory: A Modern Introduction*. Cambridge University Press, 2006.

[11] Ó. J. C. Dias, J. E. Santos, and B. Way, "Numerical Methods for Finding Stationary Gravitational Solutions," *Classical and Quantum Gravity*, vol. 33, no. 13, p. 133001, jun 2016. [Online]. Available: https://doi.org/10.1088/0264-9381/33/13/133001

[12] L. N. Trefethen, *Spectral Methods in MATLAB*. Society for Industrial and Applied Mathematics, 2000.

[13] A. Meurer, C. P. Smith, M. Paprocki, O. Čertík, S. B. Kirpichev, M. Rocklin, A. Kumar, S. Ivanov, J. K. Moore, S. Singh, T. Rathnayake, S. Vig, B. E. Granger, R. P. Muller, F. Bonazzi, H. Gupta, S. Vats, F. Johansson, F. Pedregosa, M. J. Curry, A. R. Terrel, v. Roučka, A. Saboo, I. Fernando, S. Kulal, R. Cimrman, and A. Scopatz, "Sympy: symbolic computing in python," *PeerJ Computer Science*, vol. 3, p. e103, Jan. 2017. [Online]. Available: https://doi.org/10.7717/peerj-cs.103

[14] EinsteinPy Development Team, *EinsteinPy: Python Library for General Relativity*, 2021. [Online]. Available: https:/einsteinpy.org/

[15] T. Kluyver, B. Ragan-Kelley, F. Pérez, B. Granger, M. Bussonnier, J. Frederic, K. Kelley, J. Hamrick, J. Grout, S. Corlay, P. Ivanov, D. Avila, S. Abdalla, and

C. Willing, "Jupyter Notebooks – a publishing format for reproducible computational workflows."

[16] J. Chryssathacopoulos. (2022) Analysis of Wormholes using Python. [Online]. Available: https://github.com/jchryssanthacopoulos/wormholes

[17] J. R. Culham. Elliptic Integrals, Elliptic Functions and Theta functions. [Online]. Available: http://www.mhtlab.uwaterloo.ca/courses/me755/web_chap3.pdf